Finite-size effects in a model for plasticity of amorphous composites

Botond Tyukodi,[1,2] Claire A. Lemarchand,[3,*] Jesper S. Hansen,[3] and Damien Vandembroucq[1]

[1]*Laboratoire PMMH, CNRS-UMR 7636/ESPCI/UPMC/Univ. Paris 7 Diderot, 10, rue Vauquelin, 75231 Paris cedex 05, France*
[2]*Babeş-Bolyai University, Department of Physics, 1 str. Mihail Kogălniceanu, 400084 Cluj Napoca, Romania*
[3]*DNRF Centre "Glass and Time," IMFUFA, Department of Sciences, Roskilde University, Postbox 260, DK-4000 Roskilde, Denmark*

We discuss the plastic behavior of an amorphous matrix reinforced by hard particles. A mesoscopic depinning-like model accounting for Eshelby elastic interactions is implemented. Only the effect of a plastic disorder is considered. Numerical results show a complex size dependence of the effective flow stress of the amorphous composite. In particular, the departure from the mixing law shows opposite trends associated to the competing effects of the matrix and the reinforcing particles, respectively. The reinforcing mechanisms and their effects on localization are discussed. Plastic strain is shown to gradually concentrate on the weakest band of the system. This correlation of the plastic behavior with the material structure is used to design a simple analytical model. The latter nicely captures reinforcement size effects in $(\log N/N)^{1/2}$, where N is the linear size of the system, observed numerically. Predictions of the effective flow stress accounting for further logarithmic corrections show a very good agreement with numerical results.

I. INTRODUCTION

The introduction of foreign particles into an amorphous matrix has long been used to increase the strength of disordered materials [1]. The most classical strategy consists in adding rigid particles or fibers in order to enhance the elastic properties of the composite material.

An additional or alternative strategy consists in the modification of the plastic properties. Here the effect on the overall strength is more delicate. The introduction of hard particles in a very ductile matrix tends to increase the effective yield stress and hence the strength. A good illustration of this approach can be found in the development of materials for road pavements [2–5]: Mineral micrometer scale fillers are introduced in a viscous bitumen to make it viscoplastic; the obtained mastic asphalt is then reinforced through the addition of millimetric to centimetric aggregates. More recently, the introduction of a ductile phase has been used to reinforce metallic glasses [6,7]. In this case, the ductility of the second phase enables one to control the development of shear bands, thus preventing the nucleation of cracks. A reinforcement effect is obtained despite the fact that the effective yield stress of the amorphous composite is lowered with respect to that of the matrix.

The understanding of the plastic behavior of amorphous composites thus appears to be crucial in the design of modern materials. Efforts in theoretical and numerical modeling have been recently performed to study the effects of microalloying in metallic glasses [8,9] and of the addition of aggregates in asphalt mixtures [10–12].

From the theoretical mechanics point of view, the determination of effective mechanical properties is a matter of homogenization. While this field has been intensively explored in the case of linear elastic properties [1], results are much more scarce for nonlinear behaviors like fracture [13,14] or plasticity [15–19]. In particular, standard homogenization

approaches fail to account for size effects [15,16]. Only the development of strain-gradient theories (relying on the introduction of an *ad hoc* internal length scale) has so far succeeded in reproducing size dependence [17]. Still, these approaches only predict the mean behavior and cannot cope with sample-to-sample fluctuations.

Here we develop an alternative approach, based on the recent development of depinning-like mesoscopic models of amorphous plasticity [20–25]. The modelling of amorphous plasticity and rheology of complex fluids has seen much progress in recent years [26] and a family of mesoscopic models [21,24] has emerged that rely on two main ingredients: local plastic thresholds (amorphous plasticity results from series of local rearrangements of the amorphous structure [27,28]) and account of elastic interactions (local plastic events occur in a surrounding elastic matrix and induce internal stresses [29]). These models show scaling properties close to the effective yield stress (here seen as a critical threshold) and thus exhibit statistical size effects. Another useful feature of these models is their ability to reproduce localization and shear-banding behaviors [30,31]. The effect of crystalline inclusions in an amorphous matrix has recently been discussed along such lines in Ref. [32] with a particular emphasis on the localization behavior.

Here we specialize the model recently presented in Refs. [24,33] to the case of amorphous composites by considering a bimodal distribution of local plastic stress thresholds to reproduce the inclusion of hard particles in an amorphous matrix. The simplistic model presented in the following will not be able to give a realistic account of the whole richness of the mechanical behavior of amorphous composites. However, results are expected to be generic for this class of materials.

The model is introduced in Sec. II. In Sec. III we present the complex size dependence of the yield strength measured on the amorphous matrix and amorphous composites with a growing fraction of particles. In Sec. IV, we discuss the hardening mechanisms at play in amorphous composites and the localization behavior. We emphasize in particular the interplay between the gradual localization of the plastic

*clemarch@rip.ens-cachan.fr

deformation and the building of a strongly correlated internal stress field. Elaborating on the numerical observations, we present in Sec. V an analytical model that accounts quantitatively for the size effects of the effective yield strength of amorphous composites. Mathematical details of the model are provided in a separated appendix. Our main findings are finally summarized in Sec. VI.

II. MODELLING AMORPHOUS PLASTICITY: FROM GLASSES TO AMORPHOUS COMPOSITES

The modeling of amorphous plasticity has recently given rise to an increasing interest [26]. Unlike crystalline plasticity that results from the motion of dislocations of the ordered lattice, amorphous plasticity results from series of localized rearrangements of the disordered structure [27,28,34]. Such local plastic events induce internal stresses within the surrounding material [35,36]. The latter can be seen as an elastic matrix around a plastic inclusion and the stress associated to the rearrangement computed in the spirit of the problem of the eigenstrain early introduced by Eshelby [29].

Figure 1 illustrates the analytical solution of the Eshelby problem in the far field. In this figure, the inclusion has experienced a pure shear $\varepsilon_{xx}^{\mathrm{pl}} = -\varepsilon_{yy}^{\mathrm{pl}} = \varepsilon_0^{\mathrm{pl}}$. The amplitude of the shear strain $\varepsilon = \varepsilon_{xx} - \varepsilon_{yy}$ is represented by a color scale on a reference undeformed grid (left column) and on a grid deformed according to the total displacement (right column). The first row shows the plastic strain $\varepsilon^{\mathrm{pl}}$, nonzero only within the inclusion. The second row shows the elastic strain field $\varepsilon^{\mathrm{el}}$. The latter is negative within the inclusion. Outside the inclusion it exhibits a quadrupolar symmetry: negative along the axes at $0°$ and $90°$ and positive along the directions at $\pm 45°$. The third row shows the total strain $\varepsilon = \varepsilon^{\mathrm{pl}} + \varepsilon^{\mathrm{el}}$.

The precise expression of the internal stress field σ^{el} depends on the details of the plastic strain field and the geometry of the rearranging region but, in the far field, the dominant term obeys the universal form:

$$\sigma^{\mathrm{el}} = \mu \varepsilon_0^{\mathrm{pl}} \mathcal{A} \frac{\cos(4\theta)}{r^2} , \tag{1}$$

where $\varepsilon_0^{\mathrm{pl}}$ and $\mathcal{A}$ are the mean plastic strain experienced by the inclusion and the area of the inclusion, respectively.

A. A mesoscopic model of amorphous plasticity

Following the model introduced in Refs. [21,24], the system is discretized on a two-dimensional square lattice with a lattice constant ξ. The mesoscopic length scale ξ is such that it is larger than the typical size of the plastic reorganizations, i.e., large enough to allow one to use linear elasticity but small enough to get a spatially heterogeneous local plastic field after coarse-graining. The size of the rearrangements depends on the microstructure of the material under study. In metallic glasses, results of atomistic simulations give a typical estimate about 1 nm [37]. This size is expected to be larger in polymer glasses or bitumen due to the presence of long chains. As for the convergence from discrete to continuum mechanics, it is much slower in amorphous materials than in their crystalline counterparts. While in crystals, continuum behavior is recovered after one or two interatomic distances, in
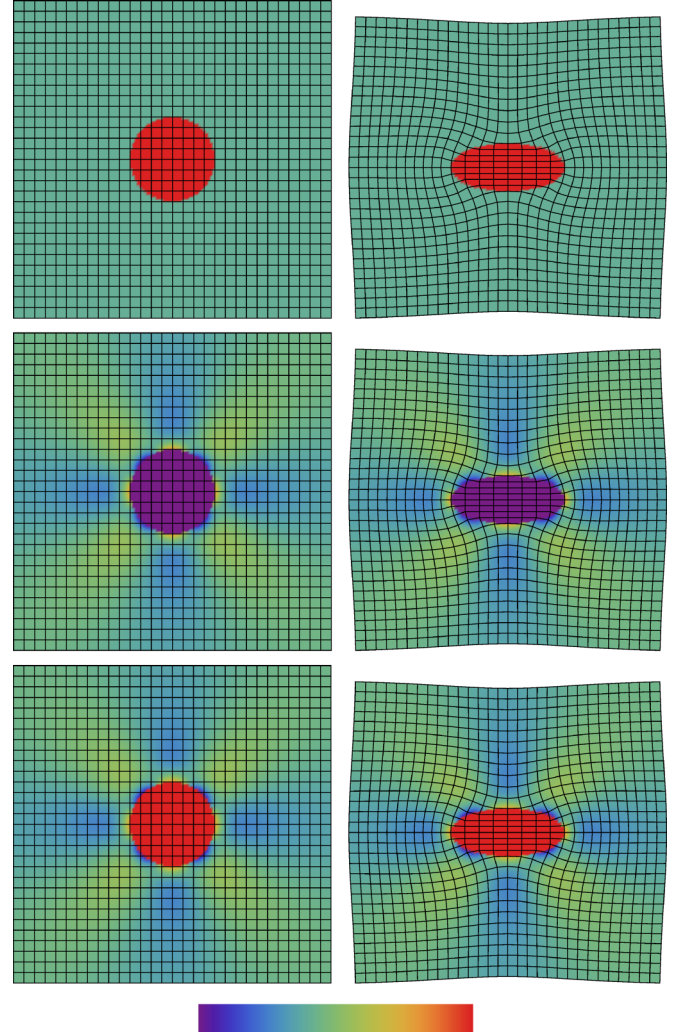

FIG. 1. Effect of a plastic inclusion in an elastic matrix submitted to a pure shear biaxial loading $\Sigma = \Sigma_{yy} = -\Sigma_{xx}$. Only the spherical inclusion experiences plasticity. The first row represents the plastic strain $\varepsilon^{\mathrm{pl}}$, the second row the elastic strain $\varepsilon^{\mathrm{el}}$, and the third row the total strain $\varepsilon = \varepsilon^{\mathrm{el}} + \varepsilon^{\mathrm{pl}}$. The strain fields are represented by a color scale on the reference mesh on the left column and on a deformed mesh on the right column. One recognizes the traditional quadrupolar symmetry associated to the Eshelby inclusion.

model metallic glasses, one has to coarse-grain upon about 5 to 20 interatomic distances to gradually recover Hooke's law, isotropy, and homogeneity (see, e.g., Ref. [38] for a detailed study). Altogether one may consider a discretization length scale of about 10 to 20 interatomic (or -molecular or -particle) distances, i.e., about a few nanometers for metallic glasses, a few tens of nanometers for polymer glasses or bitumen.

The various mechanical fields are discretized at the mesoscopic scale ξ. For each site (i,j) one can define an internal stress $\sigma_{ij}^{\mathrm{el}}$, a local plastic threshold σ_{ij}^{c}, and a local plastic strain $\varepsilon_{ij}^{\mathrm{pl}}$. A pure shear external loading is considered: $\Sigma_{xx}^{\mathrm{ext}} = -\Sigma_{yy}^{\mathrm{ext}} = \Sigma^{\mathrm{ext}}$. It is assumed that the reorganizations at a microscopic scale obey the same symmetry as the external loading, i.e., a site (i,j) undergoes a plastic deformation in pure shear: $\varepsilon_{xx}^{\mathrm{pl}} = -\varepsilon_{yy}^{\mathrm{pl}} = \varepsilon_{ij}^{\mathrm{pl}}$. A local criterion of plasticity is

considered, the elastic regime is thus defined for a site (i, j) as:

$$\Sigma^{\text{ext}} + \sigma_{ij}^{\text{el}} \leqslant \sigma_{ij}^{\text{c}} . \tag{2}$$

Values of σ^{c} are drawn from a random distribution. No spatial correlations are considered. Note here that because of elastic interactions, the plastic deformation of a site (i_0, j_0) occurs when the external stress Σ^{ext} reaches the *effective* threshold $\sigma_{i_0 j_0}^{\text{c}} - \sigma_{i_0 j_0}^{\text{el}}$. Whenever the criterion is locally satisfied the site undergoes an incremental plastic strain $\delta\varepsilon_0^{\text{pl}}$. This value is drawn from a uniform distribution in $[0, d_0]$. To account for the structural change experienced by the rearranging zone, the local plastic threshold is updated to a new value. As discussed above, the local plastic event also induces an incremental internal stress on every lattice site (i, j):

$$\delta\sigma_{ij}^{\text{el}} = G^{\text{el}} * \delta\varepsilon_0^{\text{pl}} , \tag{3}$$

where the symbol $*$ denotes the convolution operation and G^{el} is a quadrupolar kernel accounting for the elastic reaction of the matrix to a unit plastic event. Here we consider biperiodic boundary conditions and G^{el} is computed from Fourier space [24,39,40].

The system is driven with an extremal dynamics: only one site is deformed per iteration step. An iteration step corresponds to (i) identify the weakest site (i_0, j_0) for a given configuration, i.e., the site for which the *effective* local stress threshold $\sigma^{\text{c}} - \sigma^{\text{el}}$ is the lowest; (ii) update the plastic strain $\varepsilon_{i_0, j_0}^{\text{pl}}$ and the plastic threshold $\sigma_{i_0, j_0}^{\text{c}}$ at this particular site; and (iii) update the internal stress σ^{el} all over the system. A new configuration is thus obtained and the next iteration can be performed. Extremal dynamics [21] is a way of driving the system at a vanishing strain rate, in the spirit of the athermal quasistatic driving used in some atomistic simulations [41,42]. Note that the same model can be driven with other kinds of dynamics, e.g., constant stress and kinetic Monte Carlo.

A direct outcome of a simulation is the evolution of the external stress Σ^{ext} versus the average plastic strain $\langle\varepsilon^{\text{pl}}\rangle$, where the average $\langle\cdot\rangle$ represents the average over the different sites at a particular iteration step. The average plastic strain $\langle\varepsilon^{\text{pl}}\rangle$ is directly proportional to the number of iteration steps and $\langle\varepsilon^{\text{pl}}\rangle$ can be seen as a fictitious time.
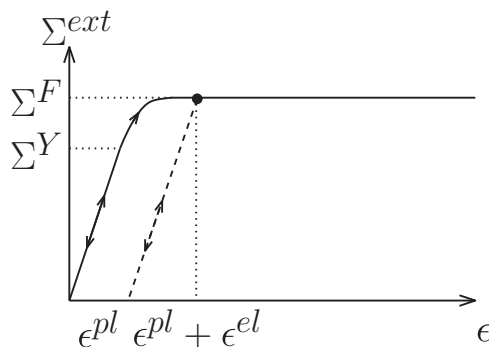

FIG. 2. Sketch of a simple plastic behavior. Plasticity sets in at yield stress Σ^{Y}, a hardening stage follows until a stress plateau is reached. The latter stress value defines the flow stress Σ^{F}. The plastic strain ε^{pl} is defined as the total strain ε minus the elastic strain ε^{el}.

In Fig. 2 we give a sketch of a simple plastic behavior. A typical stress-strain curve obtained upon monotonous loading is shown. A (reversible) elastic behavior is first observed up to the yield stress value Σ^{Y}. Above this value, plasticity sets in (a residual plastic strain is obtained upon unloading). The following curvature of the stress-strain curve is characteristic of a hardening behavior: If an unloading-loading cycle is performed, a new (larger) value of the elastic limit is obtained. A stress plateau is eventually reached that defines the ultimate flow stress Σ^{F}.

In the present framework, the external loading is not monotonous. Rather, the external stress Σ^{ext} is a fluctuating quantity which is adapted at each iteration step so that the criterion of the weakest site is satisfied. The macroscopic flow stress Σ^{F} of a given configuration is thus obtained as the maximum value of the external stress over the simulation:

$$\Sigma^{\text{F}} = \max_t \Sigma^{\text{ext}}(t), \tag{4}$$

where t is an iteration step. For an external loading $\Sigma^{\text{ext}} < \Sigma^{\text{F}}$, plastic deformation will eventually stop while any loading $\Sigma^{\text{ext}} \geqslant \Sigma^{\text{F}}$ will allow it to develop indefinitely.

B. Application to amorphous composites

The model presented above can be easily applied to the case of amorphous composites. A major hypothesis (already performed in the bare model) consists in assuming the homogeneity of the elastic properties. Only the effect of a plastic disorder will be considered in the following. To represent the amorphous composite we consider a fraction ϕ of inclusions randomly distributed in an amorphous matrix.

Here the size of the inclusions is assumed to be given by the mesh size ξ and no correlation is considered in the spatial distribution of inclusions. The fraction of inclusions is defined by $\phi = N_{\text{inc}}/N^2$ where N_{inc} is the number of hard inclusions and N the linear size of the lattice. Note that inclusions in metallic glasses [7] or filler particles in bitumen [4] can be significantly larger than the mesoscopic length scale ξ. A more realistic study would require accounting for the actual size distribution of the inclusions. However, most of the following analysis is expected to be generic enough to remain valid in these more complex cases.

A bimodal distribution is used to account for the respective plastic thresholds of the matrix and the inclusions. For the amorphous matrix, the plastic threshold is drawn from a uniform distribution $[\overline{\sigma^{\text{c}}} - \delta\sigma^{\text{c}}, \overline{\sigma^{\text{c}}} + \delta\sigma^{\text{c}}]$. Here we choose $\overline{\sigma^{\text{c}}} = 1$ and $\delta\sigma^{\text{c}} = 0.5$. The inclusions can be either less or more ductile than the amorphous matrix. In the cases of interest presented above, their nature is often crystalline. We thus assume low fluctuations of the plastic properties of the inclusions and we consider that they are characterized by a constant plastic threshold, $\sigma^{\text{c}} = \Sigma^{\text{H}}$: all inclusions get the same yield stress and this value does not change after an inclusion has experienced plastic deformation. Here we restrict the scope to the case of hard particles: $\Sigma^{H} > \overline{\sigma^{\text{c}}}$. In order to reduce the space of parameters we also consider that the typical plastic strain undergone by the inclusions is the same as in the amorphous matrix.
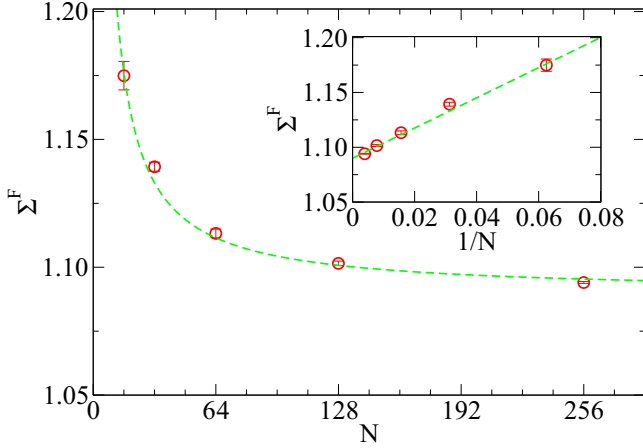
FIG. 3. Variation of the ultimate yield strength Σ^F with the system size N for a mere amorphous matrix ($\phi = 0$) with a yield stress $\sigma^c \in [0.5; 1.5]$. The line corresponds to the power-law expression $\Sigma^F = \Sigma^* + \frac{A}{N}$. As shown in the inset this evolution is consistent with the numerical data.

C. Overview of the simulations

Simulations were performed with sizes ranging from $N = 16$ up to $N = 256$ and a number $M = 40$ of independent realizations of the disorder. The fraction of inclusions was varied between $\phi = 2.5 \times 10^{-4}$ and $\phi = 0.99$. Different values of the contrast between inclusions and matrix were used: $\Sigma^H = 4, 10, 40$ and the value $\Sigma^H = 10^8$ was used to mimic infinitely hard particles. Most of the following discussion will focus on the case $\Sigma^H = 10$.

III. A SIZE-DEPENDENT EFFECTIVE YIELD STRESS

A. Amorphous matrix

We first discuss size effects in the case of a mere amorphous matrix, i.e., in the absence of hard particles. The ultimate yield strength or flow stress Σ^F of the material is defined as the maximum stress experienced by the material for a given simulation.

In Fig. 3 we show the evolution of the ultimate yield strength with the system size. A slight decrease is observed. In the inset, we show that the evolution is consistent with a simple power-law dependence:

$$\Sigma^F = \Sigma^* + \frac{A}{N}, \qquad (5)$$

where Σ^* is the flow stress in the limit of an infinitely large system and A is a constant. Such a power-law dependence is consistent with the depinning-like nature of the model. In this context [21,33,43], the plastic flow stress can be viewed as a critical threshold between a static phase (no plasticity) and a dynamic phase (plastic flow). The fluctuations of the depinning threshold measured over a finite length scale here simply reflect the divergence of the correlation length in the vicinity of a critical threshold $\xi \approx |f - f^*|^{-\nu}$. The present results are consistent with the rough estimate $\nu \approx 1$ obtained in previous works [33,43]. Figure 4 gives another illustration of this critical-like behavior. This figure shows the variation
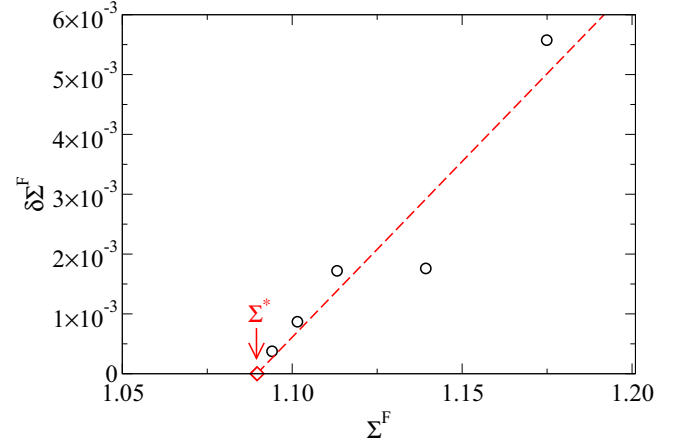

FIG. 4. Variation of the standard deviation $\delta\Sigma^F$ of the ultimate yield strength Σ^F with Σ^F for the amorphous matrix with a yield stress $\sigma^c \in [0.5; 1.5]$ for system sizes $N = 16, 32, 64, 128, 256$. The standard deviation is obtained for 40 realizations. As expected for a critical transition, a linear behavior is obtained. An extrapolation at zero standard deviation gives an estimate of the critical threshold, Σ^* at infinite size.

of the standard deviation $\delta\Sigma^F$ with the average flow stress Σ^F. The variation is reasonably reproduced by an affine relationship $\delta\Sigma^F = a(\Sigma^F - \Sigma^*)$. This is consistent with the expected critical behavior $(\Sigma^* - \Sigma^F) \propto \delta\Sigma^F \propto L^{-1/\nu}$. The intercept value Σ^* can be seen here as the extrapolated value of the effective flow stress at infinite size.

Note that, independently of the system size, the values of the effective flow stress lie significantly above the simple average of the microscopic thresholds $\overline{\sigma^c} = 1$.

B. Amorphous composites

Second, we discuss the dependence of the ultimate yield strength on the fraction of inclusions and on the size of the system.

1. Size dependence

In Fig. 5, we show the size dependence observed for amorphous composites with volume fractions of inclusions ranging from $\phi = 0$ to $\phi = 0.16$.

For low fractions of hard inclusions, the behavior is similar to that obtained for the amorphous matrix. The yield strength decreases with increasing system size and converges towards a finite value for large system sizes.

Surprisingly, the behavior markedly differs for large fractions of inclusions: The ultimate yield strength increases with increasing system size. At intermediate values of the fraction of inclusions, the evolution of the yield strength even appears to be nonmonotonic.

2. Mixing law

In Fig. 6 we show the evolution of Σ^F with the fraction ϕ of inclusions of yield stress $\Sigma^H = 10$ for system sizes ranging from $N = 16$ to $N = 256$. The error bars indicate the standard
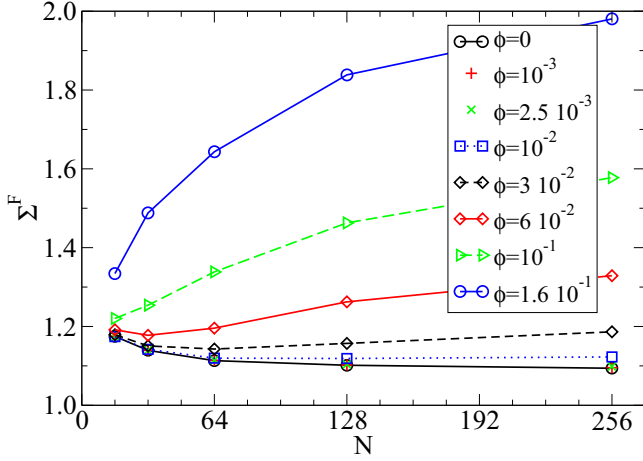
FIG. 5. Variation of the ultimate yield strength Σ^F with the system size N for the amorphous matrix ($\phi = 0$) and amorphous composites with various fractions of hard inclusions. The yield stress of the amorphous matrix is $\sigma^c \in [0.5; 1.5]$, and the yield stress of the inclusions is $\Sigma^H = 10$. Depending on ϕ the yield strength shows either a decreasing or an increasing trend with increasing system size.

deviation computed on the different realizations performed for a given pair of parameters (ϕ, N).

A clear size effect is observed. The curves obtained for different values of N do not superimpose. The larger the system, the larger the reinforcement effect induced by the hard inclusions and the closer the effective yield strength to the value obtained from a simple linear mixing law:

$$\Sigma^M(\phi, N) = (1 - \phi)\Sigma^A(N) + \phi\Sigma^H, \qquad (6)$$

where Σ^A is the ultimate yield strength of the sole amorphous matrix and Σ^H the yield stress of the hard sites. Note that the value Σ^M obtained from a linear mixing law, known
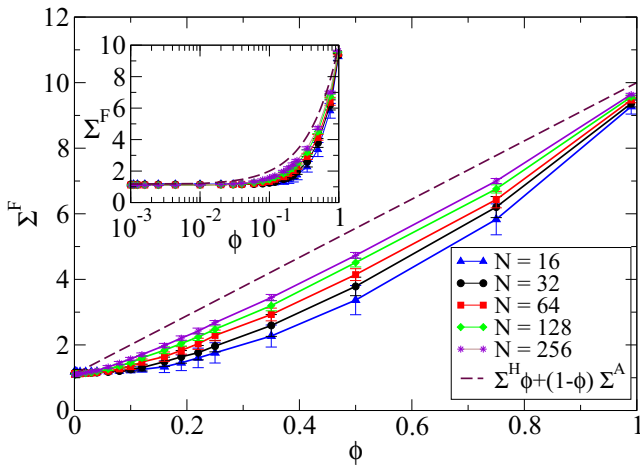

FIG. 6. Variation of the ultimate yield strength Σ^F with the fraction ϕ of hard inclusions for a yield stress $\sigma^c \in [0.5; 1.5]$ of the matrix and a yield stress $\Sigma^H = 10$ of the hard inclusions and for five different system sizes $N = 16$, $N = 32$, $N = 64$, $N = 128$, and $N = 256$. The same data are shown in the inset in semilogarithmic scale.

as the Voigt average in the context of homogenization, is usually expected to be an upper bound [1]. While this statement is true for homogenization of linear properties such as conductivity or elasticity, it does not necessarily hold for nonlinear properties such as fracture or plasticity. In the latter case, out-of-equilibrium mechanisms may allow the effective property to reach values above the Voigt bound [13,14].

Although it often fails to reproduce the experimental data quantitatively, the simple linear mixing law [44] remains widely used in material science to account for the effects of plastic reinforcement [4,45,46].

Another feature, here emphasized in the inset of Fig. 6, can be pointed out: for a given system size N, no reinforcement is observed below a threshold value $\phi_c(N)$ of the volume fraction of hard inclusions. The larger the system size N, the smaller the threshold value $\phi_c(N)$.

Despite its simplicity (scalar model, perfect plasticity), the present model is thus characterized by a complex behavior. In particular, it exhibits a clear size effect that can usually only be reproduced in the framework of more complex descriptions of plasticity such as strain-gradient-based theories [17]. A key ingredient is here the account of the elastic interaction induced by the local plastic events.

IV. HARDENING AND LOCALIZATION

We now discuss in more detail the plastic behavior of the model amorphous composites. In the following, we try to unveil the mechanisms at play in the hardening regime. We shall discriminate between two different effects, respectively associated to a structural evolution of the amorphous matrix and a concentration of the stresses on the hard particles. We then show a gradual localization of the plastic deformation on the weakest band of the material.

A. Stress-strain curves

Figure 7 displays the stress-strain curves obtained for four different values of the inclusion yield stress $\Sigma^H = 4, 10, 40, 10^8$ (the latter case being meant to mimic infinitely hard inclusions) and for different volume fractions ϕ ranging from 0 to 0.25. Note that in order to emphasize the hardening regime the variation of the stress is represented versus the sole plastic strain.

Two successive hardening regimes can be distinguished before the stress plateau corresponding to the flow stress is reached. The first one is related to the hardening of the amorphous matrix. The second one is directly induced by the presence of hard particles.

B. Statistical hardening of the amorphous matrix

In this subsection, hardening in the pure amorphous matrix is considered. At low plastic strain, a gradual hardening of the amorphous matrix takes place. This phenomenon which has been discussed in Refs. [21,24] results from the progressive exhaustion of the weakest sites of the matrix. We show in Fig. 8 the gradual evolution of the distribution of the local plastic thresholds $P(\sigma^c)$ upon deformation in the case of the sole matrix. The larger the deformation, the narrower the distribution and the closer the mean to the upper bound value.
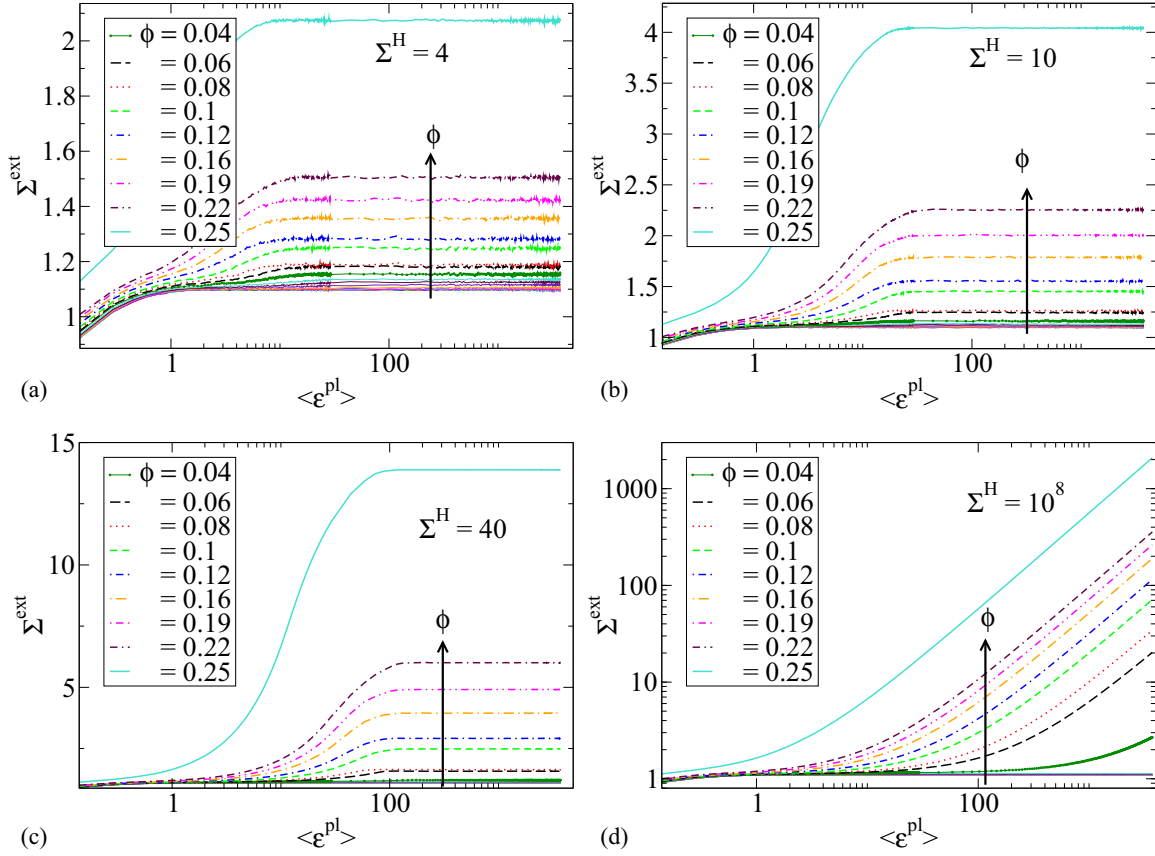
FIG. 7. Stress-strain curves for a yield stress of the matrix $\sigma^c \in [0.5; 1.5]$, a system size of $N = 64$, volume fractions of hard sites $\phi = \{0, \ldots, 0.25\}$, and for a yield stress of the hard inclusions of $\Sigma^H = 4$ (a), $\Sigma^H = 10$ (b), $\Sigma^H = 40$ (c), and $\Sigma^H = 10^8$ (d). The volume fractions which are not in the caption correspond to volume fractions below 0.06 and for which at this size the effect of adding hard inclusions is not very obvious.

This structural evolution can be understood in the following way. After plastic rearrangements, the sites are given a new plastic threshold drawn from the same random distribution
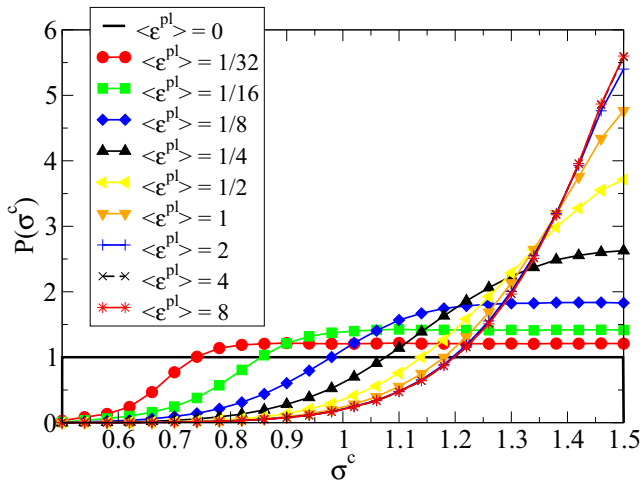

FIG. 8. Evolution of the distribution of local plastic thresholds $P(\sigma^c)$ of the pure amorphous matrix upon plastic deformation. The system studied here has size $N = 64$ and the initial yield stress of the matrix is $\sigma^c \in [0.5; 1.5]$. A gradual exhaustion effect is observed until a stationary distribution is reached.

as the initial ones. The systematic bias between the weak thresholds of the failing sites and the "normal" thresholds that replace them after deformation induces an evolutionary-like transient increase, reminiscent of self-organized criticality models [47]. It can be seen in Fig. 7 that at low fractions of inclusions, this exhaustion mechanism is the only one to hold and hard particles do not contribute to the reinforcement. Indeed the stress-strain curve at low volume fractions of hard sites is identical to that of the pure amorphous matrix.

A complementary view of this statistical hardening is given in Fig. 9. Here, instead of the local plastic thresholds, we show the evolution of the distribution of the effective thresholds $P(\sigma_c^{\text{eff}})$, where $\sigma_c^{\text{eff}} = \sigma^c - \sigma^{\text{el}}$. Indeed, following Eq. (2), the local criterion for a given site (i, j) can be rewritten as $\Sigma^{\text{ext}} \leqslant \sigma_{ij}^c - \sigma_{ij}^{\text{el}}$. In other terms, the local thresholds are dressed by the internal stress. Following the evolution of the distribution upon deformation, we recover the hardening effect. Interestingly, even in the transient stage, one can identify a sharp front associated to the lower bound of the distribution. This directly corresponds to the emergence of a yield stress. The disordered system has self-organized and in the transient stage one can unambiguously define a yield stress that depends on an internal variable, the cumulated plastic strain. This also shows the dependence of the macroscopic plastic properties on the past mechanical history.
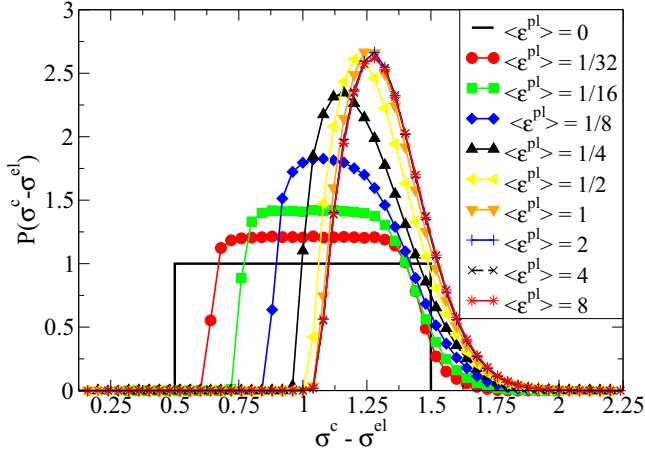
FIG. 9. Evolution of the distribution of *effective* plastic thresholds $P(\sigma_c^{\text{eff}})$ of the pure amorphous matrix, where $\sigma_c^{\text{eff}} = \sigma^c - \sigma^{\text{el}}$ upon plastic deformation. The system studied here has size $N = 64$ and the initial yield stress of the matrix is $\sigma^c \in [0.5; 1.5]$. The sharp lower front is associated to the emergence of a global yield stress. The latter gradually increases upon plastic deformation (hardening) until it reaches its final value (the stress plateau of the stress-strain curve).

C. Inclusion hardening

When hard particles are present in the amorphous matrix, an additional hardening stage is observed. As seen in Fig. 7, this second stage takes place at higher plastic strains than the matrix hardening stage. As shown in Fig. 10, this inclusion hardening regime is characterized by a linear behavior. Stress is proportional to the plastic strain until it reaches the plateau that defined the flow stress. We observe that the hardening modulus (i.e., the slope of the stress-strain curve in this hardening regime) is independent of the yield stress of the inclusions. This is evidenced in Fig. 10 (top panel) displaying the stress-strain curves obtained for an amorphous composite with 12% of inclusions. The slope remains the same, but the harder the inclusions, the longer the hardening regime. In. Fig. 10 (lower panel), we focus on the hardening regime by considering extremely hard inclusions. We clearly see that the higher the fraction of inclusions, the larger the hardening modulus. Note also that at small fractions of inclusions, the hardening modulus is vanishingly small, i.e., no reinforcing effect is obtained.

In comparison to the pure amorphous matrix, the initial distribution of plastic thresholds is bimodal in a composite. In the initial stage of the deformation, due to the high contrast of plastic thresholds, only sites of the amorphous matrix can experience plasticity. The plastic events induce internal stress. Hard particles can sustain a level of internal stress much higher than that of the amorphous matrix and act here as a kind of internal skeleton bearing most of the stress exerted on the structure.

Again it is of interest to follow the distribution of effective thresholds. In Fig. 11 we show the evolution observed for an amorphous composite with 16% of hard particles of yield stress $\Sigma^H = 10$. We see that upon plastic deformation, the buildup of internal stress on hard particles has a clear effect: It
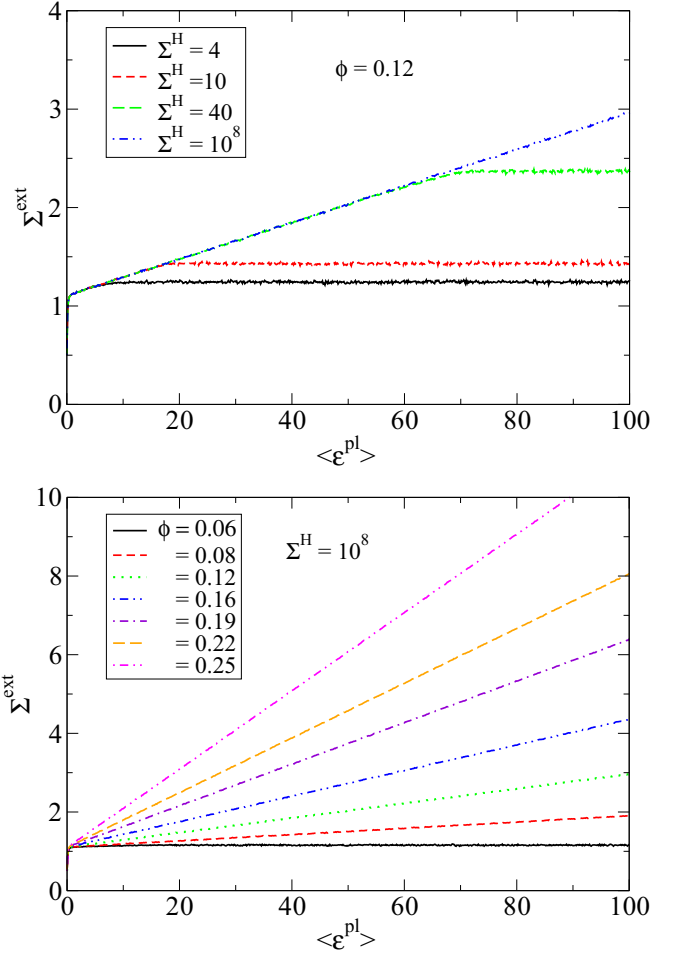

FIG. 10. Top: Stress-strain curve for amorphous composites of system size $N = 64$, with a fraction $\phi = 0.12$ of hard inclusions of yield stress $\Sigma^H = 4, 10, 40, 10^8$. The harder the inclusions, the longer the hardening regime. Bottom: Stress-strain curve for amorphous composites with a growing fraction of extremely hard particles. The higher the fraction, the larger the hardening slope.

tends to smear out the peak around $\Sigma^H = 10$. In the meantime the lower part of the distribution, in particular the sharp front that corresponds to the global yield stress, keeps on increasing. This second hardening stage is much longer than the statistical hardening of the amorphous matrix. Stationarity is eventually obtained when the second peak has entirely disappeared.

A simple mean-field argument can help us understand the reinforcing mechanism in the inclusion hardening regime. For the sake of simplicity we consider here a simple bimodal distribution with a fraction ϕ of hard inclusions of yield stress Σ^H and a fraction $(1 - \phi)$ of a soft matrix of yield stress σ_S^c. In the mean-field spirit, a site that experiences a local plastic strain increment $\delta\varepsilon_0^{\text{pl}}(t)$ at step t undergoes a local stress relaxation $\delta\sigma^{\text{el}} = -\mu\delta\varepsilon_0^{\text{pl}}(t)$ where μ is the elastic modulus while all other sites receive an additional load $\delta\sigma^{\text{el}} = \mu\delta\varepsilon_0^{\text{pl}}(t)/(N^2 - 1) \approx \mu\delta\varepsilon_0^{\text{pl}}(t)/N^2$. Consider now a series of N^2 elementary events inducing a global deformation $\langle\Delta\epsilon^{\text{pl}}\rangle = \sum_{t=1}^{N^2} \delta\varepsilon_0^{\text{pl}}(t)/N^2$, the average over all sites of the
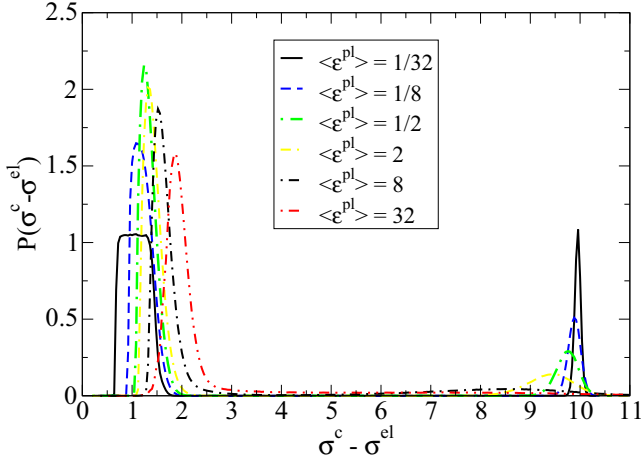
FIG. 11. Evolution of the distribution of *effective* plastic thresholds $P(\sigma_c^{\mathrm{eff}})$, where $\sigma_c^{\mathrm{eff}} = \sigma^{\mathrm{c}} - \sigma^{\mathrm{el}}$ upon plastic deformation. The system studied here has size $N = 64$ and corresponds to a volume fraction $\phi = 0.16$ of hard sites of yield stress $\Sigma^{\mathrm{H}} = 10$ and an initial yield stress of the matrix $\sigma^{\mathrm{c}} \in [0.5; 1.5]$. The building of internal stresses gradually smears out the peak associated with hard particles. Conversely, the sharp front corresponding to the global yield stress increases upon plastic deformation longer than in the case of the sole amorphous matrix.

successive microscopic deformations. Since we assume at this stage that only the amorphous matrix can experience plasticity, the typical plastic strain of an amorphous site is $\Delta\epsilon_S =$

$\langle \Delta\epsilon^{\mathrm{pl}} \rangle / (1 - \phi)$. This induces in the matrix a stress relaxation $\Delta\sigma_S^{\mathrm{rel}} = -\mu \langle \Delta\epsilon^{\mathrm{pl}} \rangle / (1 - \phi)$. We have to add to this contribution the effect of the mean-field interaction due to the other sites deforming on average of the same deformation $\langle \Delta\epsilon^{\mathrm{pl}} \rangle$: $\Delta\sigma_S^{\mathrm{int}} = \mu \langle \Delta\epsilon^{\mathrm{pl}} \rangle / N^2 \times N^2 = -(1 - \phi)\Delta\sigma_S^{\mathrm{rel}}$. The complement is borne by the hard sites $\Delta\sigma_H^{\mathrm{int}} = -\phi \Delta\sigma_S^{\mathrm{rel}}$. Altogether we get for a stress relaxation in the soft matrix: $\Delta\sigma_S^{\mathrm{el}} = -\mu\phi / (1 - \phi)\langle \Delta\epsilon^{\mathrm{pl}} \rangle$ and, conversely, a stress concentration in the hard sites. Since the local effective threshold in the matrix is $\sigma_c^{\mathrm{eff}} = \sigma_S^{\mathrm{c}} - \sigma_S^{\mathrm{el}}$ and the local plastic threshold σ_c^{c} is assumed to be constant here, we get $\Delta\sigma_c^{\mathrm{eff}} / \langle \Delta\epsilon^{\mathrm{pl}} \rangle = \mu\phi / (1 - \phi)$. We thus recover a hardening modulus that depends only on the elastic modulus and the fraction of hard sites. As will be shown later, this expression gives only a qualitative account of the dependence of the hardening modulus on ϕ.

D. Localization: No-slip bands

In order to reveal more details on the hardening mechanisms induced by the hard particles, we give a closer look at the spatial organization of the plastic strain field. In Fig. 12 we show in the top row maps of the relative plastic strain $\varepsilon_{i,j}^{\mathrm{pl}} / \langle \varepsilon^{\mathrm{pl}} \rangle$ obtained after a long simulation for three concentrations of particles ($\phi = 10^{-3}$, 10^{-2}, 10^{-1}) and in the bottom row the associated maps of plastic thresholds σ^{c} (in the final configuration of a long simulation) indicating the position of the hard sites.

The low-concentration case [Figs. 12(a) and 12(d), $\phi = 10^{-3}$] gives a good illustration of the effect of adding hard sites
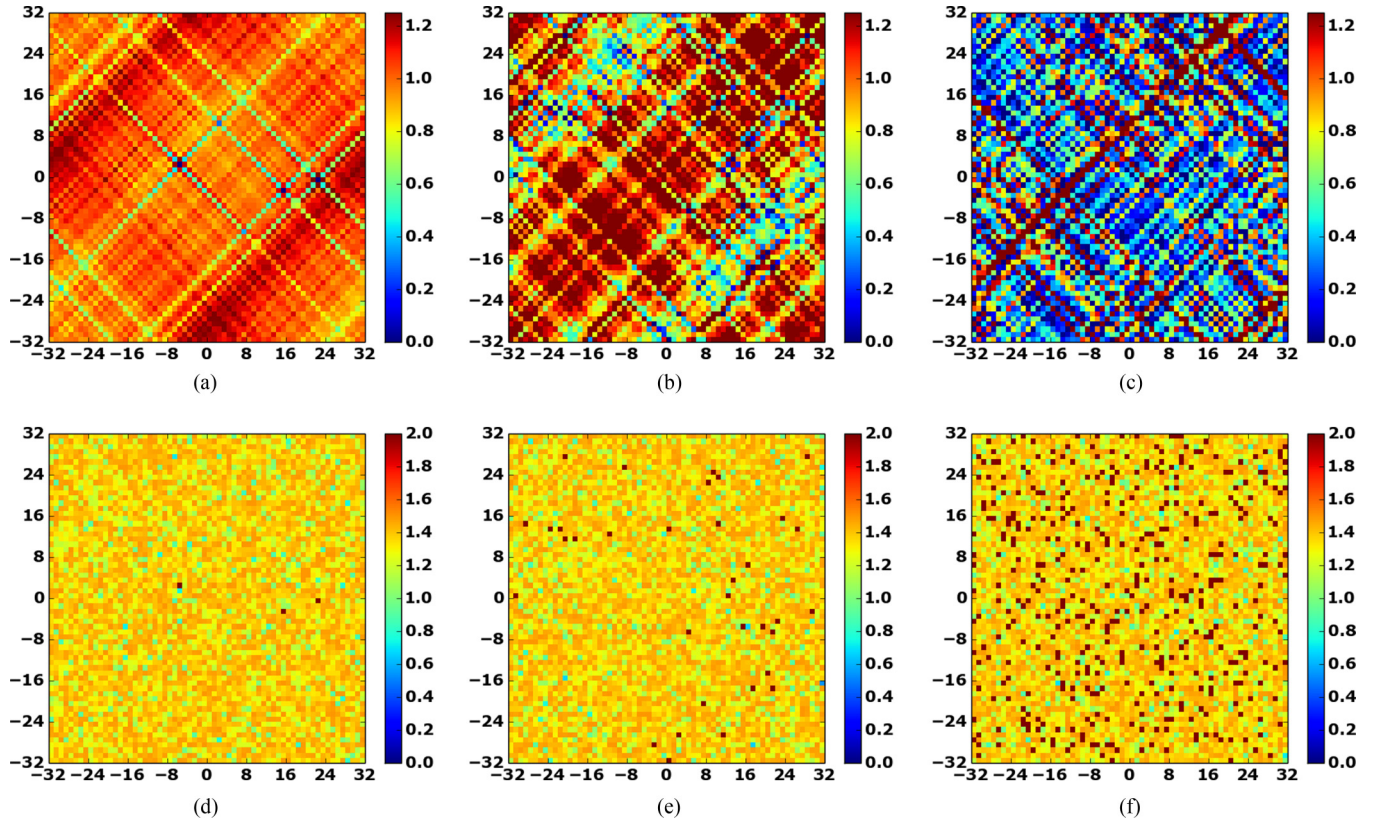

FIG. 12. [(a)–(c)] Maps of the relative plastic strain $\varepsilon_{i,j}^{\mathrm{pl}} / \langle \varepsilon^{\mathrm{pl}} \rangle$ for a system size $N = 64$, a yield stress of hard sites $\Sigma^{\mathrm{H}} = 10$, and volume fractions of hard inclusions $\phi = 10^{-3}$, 10^{-2}, 10^{-1}, respectively. The initial yield stress of the matrix is $\sigma^{\mathrm{c}} \in [0.5; 1.5]$. [(d)–(f)] Maps of the associated final configurations of plastic thresholds σ^{c}. The positions of hard sites are visible in dark red.

on plastic deformation. We see that the plastic strain field is not homogeneous. In this example where only three hard particles are present, we observe, as expected, that the hard particles are barely deformed. Interestingly, plastic deformation is also small along the bands at $\pm 45°$ that intercept the hard sites. Plasticity is inhibited along a set of "no-slip" bands induced by the presence of hard particles. These bands oriented at $\pm 45°$ obviously reflect the symmetry of the quadrupolar elastic interaction discussed above. While the low fraction of hard inclusions shown in this example is not sufficient to induce any reinforcement, it gives a simple clue on the strengthening mechanism: Hard particles inhibit the natural slip systems associated to the elastic kernel [40].

In the medium concentration case [Figs. 12(b) and 12(e), $\phi = 10^{-2}$], the (relative) plastic strain field is more heterogeneous. One recovers patterns oriented at $\pm 45°$ and it is possible to distinguish between two kinds of bands: bands containing hard sites are much less deformed than those not containing hard sites. In other words, the lattice of no-slip bands is much denser and only the sites not intercepted by these bands can easily undergo plastic deformation.

In the high-concentration case [Figs. 12(c) and 12(f), $\phi = 10^{-1}$], the (relative) plastic strain field is highly heterogeneous and highly localized. Most of the plastic deformation concentrates onto one single band. This evolution is more clearly shown in Fig. 13 where we represented maps of the incremental plastic strain $\Delta \varepsilon_{i,j}^{\text{pl}} = \varepsilon_{i,j}^{\text{pl}}(t + \delta t) - \varepsilon_{i,j}^{\text{pl}}(t)$ where δt represents a few iteration steps such that $\langle \varepsilon^{\text{pl}} \rangle(\delta t) = 2$ and

$\langle \varepsilon^{\text{pl}} \rangle(t) = 10, 20, 30, 40, 50,$ and 60. Upon deformation, plastic activity appears to become more and more localized.

E. Localization: The weakest band

We now try to correlate the plastic activity with the underlying structure, here represented by the landscape of plastic thresholds. As discussed above, plastic deformation tends to localize along bands oriented at $\pm 45°$ that reflect the symmetry of the Eshelby quadrupolar elastic interaction. Due to statistical fluctuations, not all possible slip systems encounter the same number of hard particles. We define the weakest band B_{min} and the strongest bands B_{max} as the bands containing respectively the smallest and the largest amount of hard particles among the $2N$ possible slip systems. Here we take into account the two possible orientations. Note again that we consider periodic boundary conditions so all slip systems are *a priori equivalent*. We can now compute the fraction of plastic activity occurring in the various bands. In order to highlight the gradual development of the localization, we proceed as in Sec. IV D: We consider the evolution of the incremental plastic strain field $\Delta \varepsilon_{i,j}^{\text{pl}} = \varepsilon_{i,j}^{\text{pl}}(t + \delta t) - \varepsilon_{i,j}^{\text{pl}}(t)$ with δt a few iteration steps such that $\langle \varepsilon^{\text{pl}} \rangle(\delta t) = 2$.

In Fig. 14 we show the evolution with the cumulated plastic strain $\langle \varepsilon^{\text{pl}} \rangle$ of the fractions $f_{\text{min}} = \sum_{i,j \in B\text{min}} \Delta \varepsilon_{i,j}^{\text{pl}} / \sum_{i,j=0}^{N-1} \Delta \varepsilon_{i,j}^{\text{pl}}$ and $f_{\text{max}} = \sum_{i,j \in B\text{max}} \Delta \varepsilon_{i,j}^{\text{pl}} / \sum_{i,j=0}^{N-1} \Delta \varepsilon_{i,j}^{\text{pl}}$ of the incremental plastic strain borne by the weakest and the
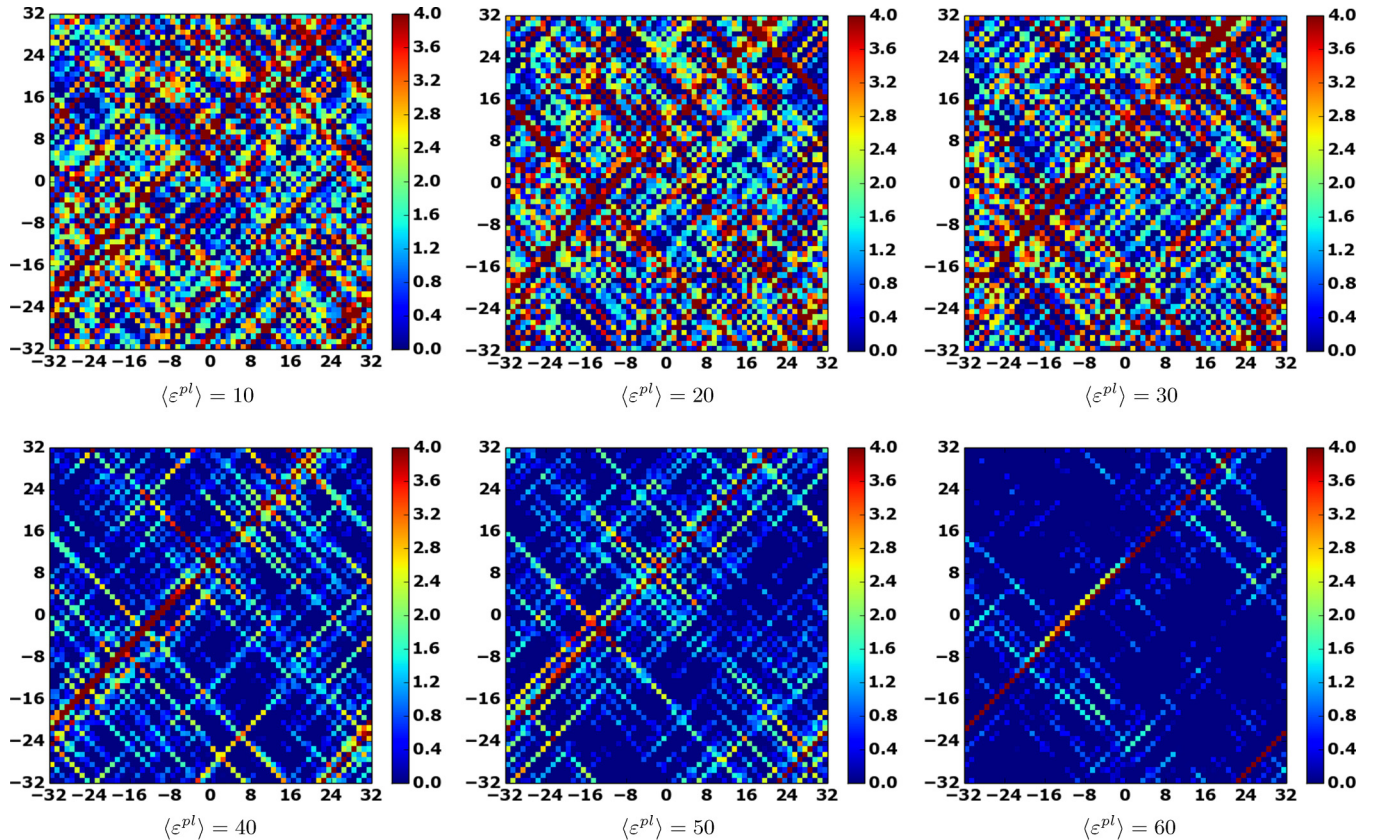

FIG. 13. Maps of incremental plastic strain $\Delta \varepsilon^{\text{pl}}$ for a volume fraction of hard inclusions $\phi = 10^{-1}$, a system size $N = 64$, a yield stress of hard sites $\Sigma^{\text{H}} = 10$, and different values of the average plastic strain $\langle \varepsilon^{\text{pl}} \rangle$.
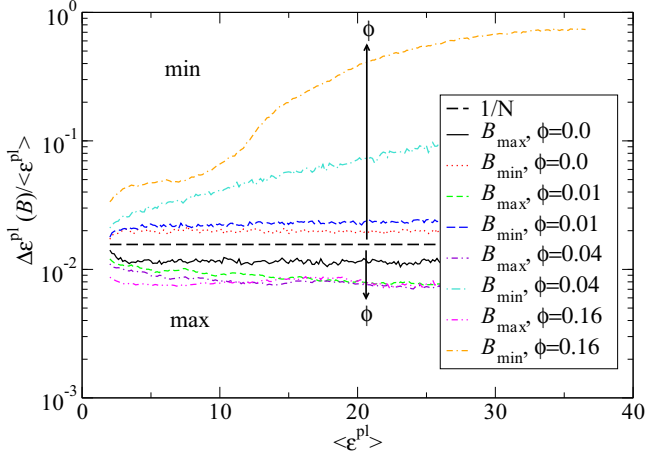
FIG. 14. Fractions $f_{\min}$ and $f_{\max}$ of incremental plastic strain $\Delta\varepsilon^{\mathrm{pl}}$ borne by the weakest and the strongest slip systems $B_{\min}$ and $B_{\max}$ containing the smallest and the largest amount of particles, respectively. The system studied here has size $N = 64$ and corresponds to a yield stress of hard sites of $\Sigma^{\mathrm{H}} = 10$.

strongest bands respectively for different concentrations of hard particles. If the plastic strain field was uniformly spread on all bands, then one would expect $f_{\min} = f_{\max} = 1/N$ (and not $1/2N$ because of the redundancy between the two possible orientations at $+45°$ and $-45°$).

In the case of the sole amorphous matrix, the weakest band deforms about twice as more than the strongest band: $f_{\min} \approx 2 f_{\max}$. For a fraction $\phi = 10^{-2}$, the effect is a bit more pronounced; we observe $f_{\min} \approx 4 f_{\max}$. This ratio remains reasonably constant upon deformation. This is consistent with the typical heterogeneity observed in Fig. 12. Note that for such a concentration the number of particles falls strictly below the number of slip systems so deformation can always find a band free of particles to develop. No significant reinforcement is expected in this case.

Above some threshold, all slip systems are virtually blocked by hard particles. This is the case for the two concentrations $\phi = 0.01$ and $\phi = 0.16$ shown in Fig. 14. Here we see a dramatic effect: upon deformation, the weakest band bears a higher and higher fraction of the plastic activity. Eventually most of the plastic strain occurs within this weakest band. We thus observe a strong correlation between structure and plastic behavior: Plastic deformation gradually concentrates onto the weakest slip system, characterized by the smallest amount of hard particles.

V. A SIMPLE ANALYTICAL MODEL

From the results above, the mechanism of reinforcement can be understood in the following way. Hard particles inhibit slip systems. No reinforcement occur until all slip systems are blocked. Above the associated threshold concentration, all slip systems are hindered by hard particles and plastic strain gradually localizes onto the weakest one, i.e., the one that contains the fewest hard particles. The macroscopic plastic behavior is thus controlled by the properties of this weakest band. In the following, we discuss these two aspects, elaborate

a simple analytical model, and compare its prediction with our simulations. Mathematical details are presented in a separated Appendix.

A. Percolation

As discussed above, no reinforcement is expected until all slip systems are blocked by at least one particle. Here the two families of slip systems associated to the two directions at $\pm 45°$ should *a priori* be considered. For the sake of simplicity, we consider in the following only one of the two orientations. This approximation allows us to recover a simple one-dimensional percolation problem.

We assume here that the distribution of particles is not spatially correlated and take the volume fraction ϕ as the probability for one inclusion to be hard. The probability to have exactly n hard inclusions in one randomly chosen diagonal is then a binomial distribution:

$$P(N_d = n) = \binom{N}{n}\phi^n(1-\phi)^{N-n} , \tag{7}$$

where N_d is the random variable counting the number of hard sites on a diagonal, $N_d = n$ is the event "n hard sites on a diagonal," and N is the number of sites in a diagonal, which is exactly the system size in the square lattice considered here. The probability of having at least one hard inclusion on a diagonal is

$$P(N_d \geqslant 1) = 1 - (1-\phi)^N. \tag{8}$$

There are N diagonals with the same orientation. They are independent. Consequently, the probability to have at least one hard inclusion on each diagonal is

$$P(B) = (1 - (1-\phi)^N)^N, \tag{9}$$

where the letter B stands for "blocked." This probability is the equivalent of the probability of percolation. It is plotted for different system sizes versus the volume fraction of hard inclusions in Fig. 15. The probability of having at least one
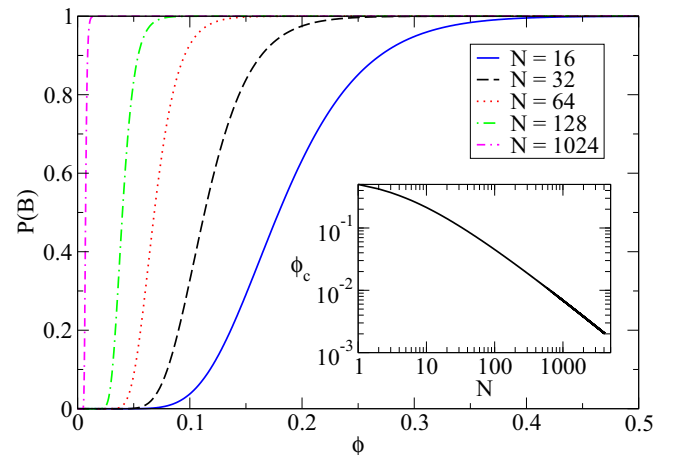

FIG. 15. Variation of the probability $P(B)$ of having at least one hard inclusion on each diagonal, defined in Eq. (9), with the volume fraction ϕ of hard inclusions for different system sizes $N = 16$, $N = 32$, $N = 64$, $N = 128$, $N = 1024$. Inset: Variation of the critical fraction ϕ_c defined in Eq. (10) with the system size N.
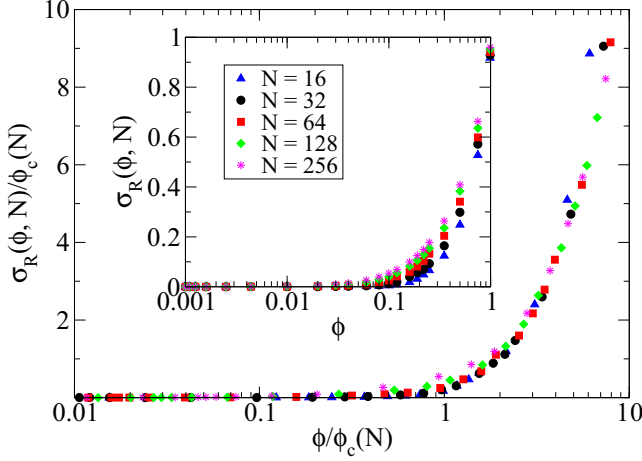
FIG. 16. Variation of the rescaled yield strength $(\Sigma^{\mathrm{F}}(\phi,N) - \Sigma^{\mathrm{A}})/(\Sigma^{\mathrm{H}} - \Sigma^{\mathrm{A}})/\phi_c(N)$ with the rescaled volume fraction $\phi/\phi_c(N)$ for a yield stress $\Sigma^{\mathrm{H}} = 10$ of hard inclusions and different system sizes $N = 16, 32, 64, 128, 256$. Inset: Variation of $[\Sigma^{\mathrm{F}}(\phi,N) - \Sigma^{\mathrm{A}}]/(\Sigma^{\mathrm{H}} - \Sigma^{\mathrm{A}})$ with ϕ for the same systems.

hard inclusion per diagonal increases with the volume fraction of hard inclusions until it reaches 1.

The threshold for percolation, or here for all diagonals to be blocked, is the volume fraction ϕ for which the probability $P(B)$ is the steepest. In other words, the threshold for the transition corresponds to the volume fraction of hard inclusions for which the second derivative of $P(B)$ vanishes. This volume fraction is called critical and denoted ϕ_c. It is equal to

$$\phi_c(N) = 1 - \frac{1}{(N+1)^{1/N}}. \tag{10}$$

The inset of Fig. 15 shows the variation of the critical fraction ϕ_c with the system size N.

To illustrate the thresholding effect, one can define the rescaled flow stress $\sigma_R(\phi,N)$ as the reinforcement factor with respect to the flow stress of the amorphous matrix:

$$\sigma_R(\phi,N) = \frac{\Sigma^{\mathrm{F}}(\phi,N) - \Sigma^{\mathrm{A}}(N)}{\Sigma^{\mathrm{H}} - \Sigma^{\mathrm{A}}(N)}. \tag{11}$$

Figure 16 shows the ratio $\sigma_R(\phi,N)/\phi_c(N)$ versus the rescaled volume fraction $\phi/\phi_c(N)$ for different system sizes. This plot is to be compared with the inset of Fig. 16 showing the same quantities without the rescaling by $\phi_c(N)$. In the main plot, the curves corresponding to different system sizes collapse onto a single master curve, showing that our interpretation of the transition is valid.

B. Yield stress of the weakest band

1. Restriction to elastic line depinning

In Sec. IV, plastic deformation was shown to concentrate onto one single band, the one containing the smallest amount of hard particles. It is thus natural to use the ultimate yield strength of that weakest band as an estimate for the ultimate yield strength of the whole amorphous composite. Ignoring the residual plastic strain undergone outside the band, the problem is thus reduced to a one-dimensional elastic depinning problem

very similar to the propagation of a crack front in a random landscape [14,48].

Indeed, if we denote $\varepsilon_i^{\mathrm{W}} = \varepsilon^{\mathrm{W}}(z_i)$ the plastic strain in the weakest band at location z_i where z is the distance along the band, then any local plastic strain increment $\delta\varepsilon_i^{\mathrm{W}}$ induces along the band an internal stress proportional to an elastic kernel which is nothing but the restriction on a diagonal of the Eshelby quadrupolar stress defined in Eq. (1). More specifically the internal stress at location z_j induced by the plastic strain increment at location z_i amounts to:

$$\delta\sigma_{ii}^{\mathrm{W}} = -A_0\varepsilon_i^{\mathrm{W}},$$
$$\delta\sigma_{ij}^{\mathrm{W}} = \frac{A_1}{(z_i - z_j)^2}\varepsilon_i^{\mathrm{W}}, \quad \text{if} \quad i \neq j, \tag{12}$$

where A_0 and A_1 are positive constants. One recognizes here the elastic interaction associated to the trapping of an interfacial crack front [49].

The determination of the effective toughness of an interfacial crack propagating in a random landscape (which also amounts to the critical threshold of a long-range elastic line) has recently been discussed in Ref. [14]. While the effective toughness can significantly exceed the simple arithmetic average of the microscopic properties when the disorder is highly fluctuating in the direction of propagation (strong pinning), a simple mixing law is recovered when the microscopic toughness is only slowly varying along the direction of propagation (weak pinning).

In the present case, the hard sites are persistent, i.e., the value of their yield stress does not change upon deformation. Besides, the fluctuations of the local thresholds that characterize the amorphous matrix are weak compared with the yield stress of the hard sites. Weak pinning conditions can thus be considered and a simple mixing law used to compute the effective yield stress of the band.

2. How weak is the weakest band?

The effective yield stress of the weakest band σ_Y^W is thus simply written:

$$\Sigma^{\mathrm{W}} = \frac{N-m}{N}\Sigma^{\mathrm{A}} + \frac{m}{N}\Sigma^{\mathrm{H}}, \tag{13}$$

where Σ^{A} is the yield stress of the amorphous matrix and Σ^{H} that of the hard sites and m is the number of hard sites in the band. The estimate of the ultimate yield strength Σ^{F} of the material is given by the ensemble average:

$$\Sigma^{\mathrm{F}} = \langle\Sigma^{\mathrm{W}}\rangle = \frac{N - \langle m\rangle}{N}\Sigma^{\mathrm{A}} + \frac{\langle m\rangle}{N}\Sigma^{\mathrm{H}}, \tag{14}$$

where $\langle m\rangle$ is the average minimum number of hard sites on a diagonal of size N for a fraction ϕ of hard sites. In the following we define $f = \langle m\rangle/N$, the effective fraction of hard sites in the weakest band. As it immediately appears from Eq. (14), within the weakest band approximation, the difference between the effective flow stress Σ^{F} and the mixing law estimate Σ^{M} directly stems from the difference between f and ϕ.

The distribution of the number m of hard sites is given by the binomial distribution of parameters ϕ and N. An exact formula for the average $\langle m\rangle$ of the minimal number of hard

sites on a diagonal when N diagonals are considered is given in the Appendix. However, this formula contains an infinite sum and is not easy to handle. In order to estimate this minimal value we shall resort to an argument of extremal statistics. Depending on the value of ϕ, the binomial converges at large N either to a Gaussian or to a Poisson distribution. In the present case we are interested in the large deviations of the binomial distribution [50]. We use recent results on the general approximation of the binomial distribution [51,52] obtained in the context of cryptology studies:

$$P(m \leqslant fN) = \frac{\phi\sqrt{1-f}}{(\phi-f)\sqrt{2\pi Nf}}e^{-ND(f\|\phi)}, \quad (15)$$

for $N \to \infty$ where $D(f\|\phi)$ is the Kullback-Leibler divergence defined as:

$$D(f\|\phi) = f \ln \frac{f}{\phi} + (1-f) \ln \frac{1-f}{1-\phi}. \quad (16)$$

Here the fraction f of hard sites in the weakest band is estimated via a simple extremal statistics argument:

$$P(m \leqslant fN) \approx \frac{1}{N}. \quad (17)$$

Detailed calculations based on the asymptotic expansions given in Ref. [52] are presented in the Appendix. They allow us to obtain an estimate of the distance between the fraction f (the fraction of hard sites in the weakest band) and the parameter ϕ of the binomial distribution (the mean fraction of hard sites):

$$f = \phi - \sqrt{\frac{2\phi(1-\phi)}{N}\log\frac{N}{\sqrt{2\pi}}}(1+r_N), \quad (18)$$

where

$$r_N = -\frac{1}{2}\frac{\log(2h_N)}{2h_N+1}, \quad h_N = \log\frac{N}{\sqrt{2\pi}}. \quad (19)$$

C. Effective plastic behavior

1. Size scaling of the flow stress

This immediately sets the distance of the flow stress Σ^F to the mixing law value $\Sigma^M(\phi,N)$ obtained by Eq. (6):

$$\Sigma^F(\phi,N) = \Sigma^M(\phi,N) - (\phi-f)[\Sigma^H - \Sigma^A(N)]. \quad (20)$$

In particular we obtain a clear size effect: The convergence to the mixing law scales as $(\log N/N)^{1/2}$. This result is illustrated in Fig. 17 where we display the variation of the rescaled flow stress $\sigma_R(\phi,N)$ with $(\log N/N)^{1/2}$ for various values of the fraction ϕ of hard sites. The rescaled flow stress $\sigma_R(\phi,N)$ is defined as in Eq. (21) as the reinforcement factor with respect to the flow stress of the amorphous matrix:

$$\sigma_R(\phi,N) = \frac{\Sigma^F(\phi,N) - \Sigma^A(N)}{\Sigma^H - \Sigma^A(N)}. \quad (21)$$

In the framework of our approximation, we expect $\sigma_R(\phi,N) = f(\phi,N)$, where $f(\phi,N)$ is the lowest fraction of hard inclusions among all bands. In particular, following Eq. (18), we should recover $\phi - \sigma_R(\phi,N) \propto (\log N/N)^{1/2}$. As shown in Fig. 17, this scaling is nicely obeyed for moderate values of ϕ. Departures from the predicted scaling behavior become
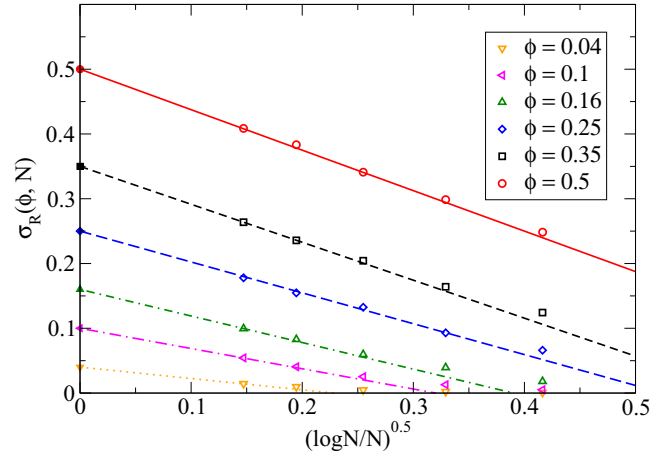

FIG. 17. Size scaling of the rescaled flow stress $\sigma_R(\phi,N)$, defined in Eq. (21), of amorphous composites with concentration of hard particles ranging from $\phi = 0.04$ to $\phi = 0.5$. The yield stress of hard sites is $\Sigma^H = 10$. Filled symbols on the vertical axis correspond to the infinite size limit, i.e., the result of the mixing law. The lines indicate the expected scaling behavior in $(\log N/N)^{1/2}$.

significant at low values of ϕ and N, because the analytical estimation holds only in the limit of large N and intermediate values of ϕ. A numerical estimation of the average number $\langle m \rangle$ of hard sites in the weakest band is discussed in the Appendix and shows that the approximation holds surprisingly well even for low values of ϕ and small system sizes.

Beyond the prediction of the scaling behavior, the logarithmic corrections accounted for in Eq. (18) allow us to test quantitatively our predictions for the reinforcement effect of hard inclusions in an amorphous matrix. In Fig. 18 we compare analytical predictions and simulation results for the rescaled flow stress $\sigma_R(\phi,N)$ with respect to the fraction of hard sites
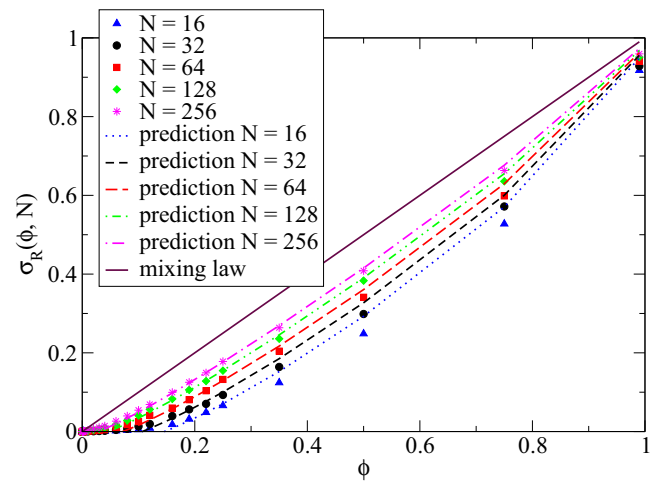

FIG. 18. Effect of the concentration of hard particles on the rescaled flow stress of amorphous composites for different system sizes $N = 16, 32, 64, 128, 256$. The yield stress of hard sites is $\Sigma^H = 10$. The straight line corresponds to the mixing law expected at infinite size. The dashed lines are the analytical predictions of Eq. (21) accounting for logarithmic corrections.
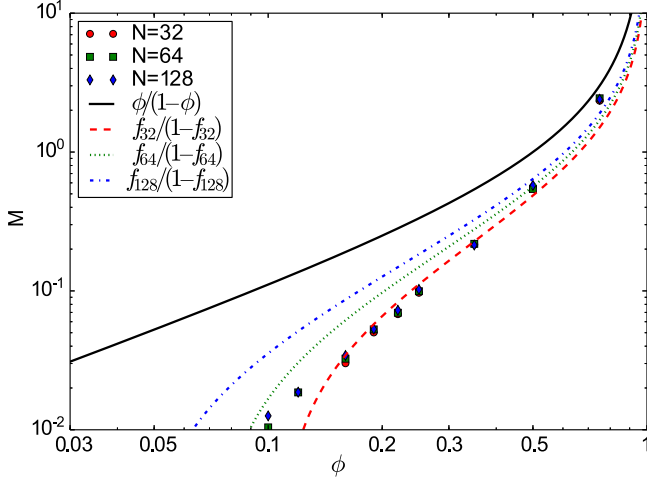
FIG. 19. Hardening modulus versus fraction of hard sites for system sizes $N = 64, 128, 256$ (symbols). The continuous line shows the mean-field expression $M(\phi) = \phi/(1 - \phi)$ and the discontinuous lines the size-dependent prediction $M(\phi, N) = f(\phi, N)/[1 - f(\phi, N)]$ where f is the fraction of hard sites in the weakest band.

ϕ. Again, our prediction of effective flow stress happens to be very precise for moderate values of ϕ and large system sizes.

2. Scaling behavior of the hardening regime

The above analysis also enables us to better understand the hardening regime. The simple mean-field argument developed in Sec. IV gives for the hardening modulus $M = d\Sigma^{\text{ext}}/d\langle\Delta\epsilon^{\text{pl}}\rangle = \mu\phi/(1 - \phi)$. As shown in Fig. 19, this expression (that does not account for size effects) widely overestimates numerical observations.

In order to go a step further we propose here a slightly more elaborated argument relying again on the localization of the plastic activity onto the weakest band. This assumption motivates us to build a simple elastic interaction obeying a quadrupolar symmetry. Namely, for a system of size N we consider the following discretized kernel $G_{i,j}$ on each site i, j:

$$
\begin{aligned}
G_{0,0} &= -1 \\
G_{i,i} = G_{i,-i} &= \frac{1}{N-1} \approx \frac{1}{N} \\
G_{0,i} = G_{i,0} &= \frac{-1}{N-1} \approx \frac{-1}{N} \\
G_{i,j} &= \frac{-1}{N^2 - 4(N-1)} \approx \frac{1}{N^2},
\end{aligned}
\tag{22}
$$

This kernel corresponds to a stress relaxation in the center and in the bands at $0°$ and $90°$, to an internal stress creation in the bands at $\pm45°$, and to a mean-field internal stress creation in the rest of the system. For this simple kernel, as for the Eshelby quadrupolar kernel, a homogeneous deformation along a line at $\pm45°$ induces no internal stress, in other terms, shear bands at $\pm45°$ are soft modes of the elastic kernel [40]. Along one band one recovers a one-dimensional mean-field interaction: a unit stress drop in the deformed site, and a constant increase $1/(N-1) \approx 1/N$ on the other sites of the band.

Let us now consider a set of N bands, each of them experiencing a mean plastic strain ε_i, $i \in [1, N]$. In the following we consider the different bands as noninteracting, i.e., we neglect the stress noise due to the nonhomogeneity of the plastic strain of distant bands. The contrast between soft and hard sites is only considered within the band of interest. Along the band i of fraction f_i of hard sites, the plastic strain is borne only by the soft sites. The latter thus undergo a plastic strain $\varepsilon_i/(1 - f_i)$. This induces in return an internal stress $\Delta\sigma_{i,S}$ in the soft sites and $\Delta\sigma_{i,H}$ in the hard sites:

$$
\begin{aligned}
\Delta\sigma_{i,S} &= -\frac{1}{1 - f_i}\mu\varepsilon_i + \mu\varepsilon_i \\
&= -\frac{f_i}{1 - f_i}\mu\varepsilon_i
\end{aligned}
\tag{23}
$$

$$
\Delta\sigma_{i,H} = \mu\varepsilon_i,
$$

where the two contributions for the soft sites correspond respectively to the stress relaxation and the mean-field interaction along the band. Along each of the bands, the soft sites thus undergo a stress relaxation whose amplitude depends on the fraction of hard sites f_i. The lower f_i, the lower the stress relaxation and the lower the increase of the plastic criterion $\Delta(\sigma_S^c - \sigma_{i,S}) = -\Delta\sigma_{i,S}$. Imposing an increment of external stress $\Delta\Sigma^{\text{ext}} = \Delta(\sigma_S^c - \sigma_{i,S})$ we thus get in the band a plastic strain:

$$
\varepsilon_i = \frac{1 - f_i}{f_i}\frac{\Sigma^{\text{ext}}}{\mu}.
\tag{24}
$$

Averaging over different bands i, we get:

$$
\begin{aligned}
\langle\varepsilon\rangle &= \left\langle\frac{1 - f_i}{f_i}\right\rangle\frac{\Sigma^{\text{ext}}}{\mu} \\
&\approx \frac{1 - f}{f}\frac{\Sigma^{\text{ext}}}{\mu} \quad \text{if} \quad f = \min(f_i) \ll \langle f_i\rangle.
\end{aligned}
\tag{25}
$$

In the vicinity of the threshold $\phi_c(N)$ above which a reinforcement is observed, we thus expect a hardening modulus controlled by the fraction f of hard sites in the weakest band: $M(\phi, N) = f/(1 - f)$ significantly smaller than the mean-field value $\phi/(1 - \phi)$. Numerical results are compared with these expressions for different system sizes in Fig. 19 and show a reasonable agreement.

Finally, using the scaling of the plateau stress given in Eq. (21) and the above estimate of the hardening modulus we can propose an estimate for the plastic strain $\langle\epsilon_{\text{hr}}^{\text{pl}}\rangle$ of the hardening regime:

$$
\begin{aligned}
\langle\epsilon_{\text{hr}}^{\text{pl}}\rangle &= \frac{\Sigma^{\text{F}}(\phi, N) - \Sigma^{\text{A}}(N)}{M(\phi, N)} \\
&\approx \frac{\Sigma^{\text{H}} - \Sigma^{\text{A}}(N)}{\mu}[1 - f(\phi, N)]
\end{aligned}
\tag{26}
$$

and we get finally:

$$
\frac{\mu\langle\epsilon_{\text{hr}}^{\text{pl}}\rangle}{\Sigma^{\text{H}} - \Sigma^{\text{A}}(N)} \approx 1 - \phi + \sqrt{\frac{2\phi(1 - \phi)}{N}\log\frac{N}{\sqrt{2\pi}}},
\tag{27}
$$

where for simplicity we did not account for the logarithmic corrections of Eq. (18).

VI. CONCLUSION

The plastic behavior as described in the mesoscopic simulations shows two types of system-size dependence. The first type corresponds to an effect of the amorphous matrix only and results from the critical character of the yielding transition. In this case, the ultimate yield strength decreases with an increasing system size, as $1/N$. This system-size dependence has already been addressed in Refs. [33,43]. A similar critical behavior has recently been advocated in the related framework of compressive strength of brittle heterogeneous materials [53].

The second type of size effect is specific to the composite material. Below a critical volume fraction of hard inclusions depending on the system size, no hardening behavior of the second type is observed. Above this critical volume fraction, the hardening behavior depends on the system size: The ultimate yield strength increases with an increasing system size, as $-(\log N/N)^{1/2}$. We showed that the thresholding effect observed in the simulations is close to a percolation transition. We also showed that during this second hardening regime, most of the plastic strain is concentrated onto the weakest band. Therefore, we proposed a simple model to describe the dependence of the ultimate yield strength Σ^{F} on the system size and the volume fraction. This model is based on the assumption that the weakest band bears all the plastic strain and governs the ultimate yield strength Σ^{F} of the entire system. The ultimate yield strength Σ^{F} is then given by a combination of the yield strength of the pure matrix and of the hard inclusions, weighted respectively by the fraction of matrix sites and of hard inclusions in the weakest band. Using extremal statistics arguments, we proposed an analytical estimate of the average number of hard inclusions in the weakest band in the limit of large system sizes. The comparison of the analytical estimate with the simulation results is satisfactory and our model, consequently, makes a direct link between the structure, represented by the plastic threshold on each site, and the mechanical behavior.

ACKNOWLEDGMENTS

APPENDIX: ANALYTICAL APPROACH

1. Exact formula

To obtain an exact formula for the average minimum number $\langle m \rangle$ of inclusions per diagonal, we use its definition:

$$\langle m \rangle = \sum_{n=0}^{N} n P(m=n),$$

$$= \sum_{n=1}^{N} n P(m=n). \tag{A1}$$

The variable n in this expression can be reformulated as a sum:

$$\langle m \rangle = \sum_{n=1}^{N} \sum_{k=0}^{n-1} P(m=n),$$

$$= \sum_{k=0}^{N-1} \sum_{n=k+1}^{N} P(m=n), \tag{A2}$$

where the indices in the two sums are enumerated in two different and equivalent ways. The sum over the index n can then be contracted into:

$$\langle m \rangle = \sum_{k=0}^{N-1} P(m \geqslant k+1),$$

$$= \sum_{n=1}^{N} P(m \geqslant n),$$

$$= \sum_{n=1}^{N} (P(N_d \geqslant n))^N,$$

$$= \sum_{n=1}^{N} (I_\phi(n, N-n+1))^N, \tag{A3}$$

where N_d is the random variable counting the number of hard sites in a diagonal and I_ϕ the regularized incomplete β function. The regularized incomplete β function is used here to express the cumulative distribution of the binomial distribution. The last formula of Eq. (A3) is explicit but hard to evaluate for large values of N.

2. Analytical estimation

To obtain an analytical estimate of the average minimum number $\langle m \rangle$ of inclusions per diagonal, we use a result from extreme value theory on the minimum of N independent and identically distributed random variables:

$$P(N_d \leqslant \langle m \rangle) = \frac{1}{N}, \quad N \to \infty, \tag{A4}$$

where N_d is the random variable counting the number of inclusions in any diagonal. In our case, the diagonal have N sites. We introduce the ratio $f = \langle m \rangle / N$ convenient in the limit of large N and Eq. (A4) becomes:

$$P(N_d \leqslant fN) = \frac{1}{N}, \quad N \to \infty. \tag{A5}$$

As the random variable N_d has a binomial distribution with parameters N and ϕ, we can employ a result of cryptography given in Refs. [51,52]:

$$P(N_d \leqslant fN) = \frac{\phi\sqrt{1-f}}{(\phi-f)\sqrt{2\pi Nf}} e^{-ND(f||\phi)}, \tag{A6}$$

for $N \to \infty$ where $D(f||\phi)$ is the Kullback-Leibler divergence defined as:

$$D(f||\phi) = f \ln \frac{f}{\phi} + (1-f) \ln \frac{1-f}{1-\phi}. \tag{A7}$$

We then introduce $\epsilon = \phi - f$; and ϵ is expected to tend to 0 in the limit of large N, i.e., f tends to ϕ in the limit of large N.

Using Eqs. (A5) and (A6) and another result from Refs. [51,52] on the behavior of the Kullback-Leibler divergence valid for $O(\epsilon) = O(\epsilon/\phi) = O[\epsilon/(1-\phi)]$:

$$D(\phi - \epsilon || \phi) = \frac{\epsilon^2}{2\phi(1-\phi)} + O(\epsilon^3), \qquad (A8)$$

we obtain:

$$\frac{1}{N} = \frac{\phi\sqrt{1-\phi+\epsilon}}{\epsilon\sqrt{2\pi N(\phi-\epsilon)}} e^{-\frac{N\epsilon^2}{2\phi(1-\phi)}}. \qquad (A9)$$

To first order in ϵ, this becomes:

$$\frac{1}{N} = \frac{1}{\sqrt{2\pi}} \frac{\sqrt{\phi(1-\phi)/N}}{\epsilon} e^{-\frac{N\epsilon^2}{2\phi(1-\phi)}}, \qquad (A10)$$

We define $\epsilon' = \epsilon/\sqrt{\phi(1-\phi)/N}$ and Eq. (A10) is equivalent to

$$\epsilon'^2 = 2\ln\frac{N}{\sqrt{2\pi}\epsilon'}. \qquad (A11)$$

To obtain an approximate solution to this transcendental equation, we define the variable r such that:

$$\epsilon' = \sqrt{2h_N}(1+r), \qquad (A12)$$

where $h_N = \ln\frac{N}{\sqrt{2\pi}}$. The variable r tends to 0 in the limit of large N. We also have:

$$\epsilon'^2 = 2h_N(1+r)^2 = 2h_N(1+2r) + \mathcal{O}(r^2), \qquad (A13)$$

to first order in r. Using the transcendental equation (A11) and iterating once in ϵ, we get:

$$\epsilon'^2 = 2\ln\frac{N}{\sqrt{2\pi}\sqrt{2h_N}(1+r)}. \qquad (A14)$$

Equating the right-hand sides of Eqs. (A13) and (A14) leads to:

$$2h_N(1+2r) = 2\ln\frac{N}{\sqrt{2\pi}\sqrt{2h_N}(1+r)},$$
$$= 2\ln\frac{N}{\sqrt{2\pi}\sqrt{2h_N}} - 2\ln(1+r),$$
$$= 2\ln\frac{N}{\sqrt{2\pi}\sqrt{2h_N}} - 2r, \qquad (A15)$$

to first order in r. The last line of Eq. (A15) is a linear equation in r, and its solution reads:

$$r = \frac{\ln\frac{N}{\sqrt{2\pi}\sqrt{2h_N}} - h_N}{2h_N + 1}. \qquad (A16)$$

Finally, the ratio $f = \langle m \rangle/N$ can be expressed in terms of $r(N)$:

$$f = \phi - \sqrt{\frac{\phi(1-\phi)}{N}}\sqrt{2h_N}[1+r(N)]. \qquad (A17)$$

The solution given in Eq. (A17) can be checked numerically. The function g is defined by:

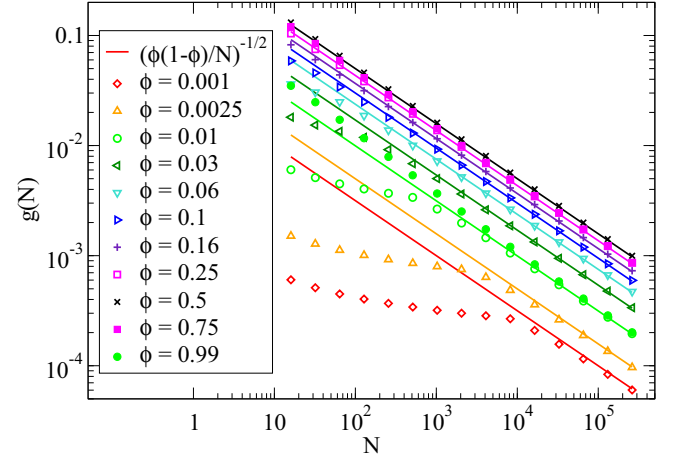$$g(N) = \frac{\phi - f}{1+r(N)}\frac{1}{\sqrt{2h_N}}. \qquad (A18)$$

FIG. 20. Variation of the function $g(N) = (\phi - f)/(1 + r(N))/\sqrt{2h_N}$ with N for different values of ϕ. The opened symbols correspond to a numerical evaluation of $g(N)$ using 10 000 iterations of N drawings from a binomial distribution with parameters N and ϕ. The solid and opened symbols of the same color and shape correspond to results for ϕ and $(1 - \phi)$, respectively. The solid lines correspond to the analytical estimation given in Eq. (A19) in the limit of large N.

According to Eq. (A17), it is equal to

$$g(N) = \sqrt{\frac{\phi(1-\phi)}{N}}. \qquad (A19)$$

Figure 20 displays the function g as obtained for 10 000 numerical iterations of N drawings from a binomial distribution with parameters N and ϕ for different values of N and ϕ. The analytical estimation of $g(N)$ given in Eq. (A19) works very well down to $N = 16$ for values of ϕ in $0.1 \leqslant \phi \leqslant 0.9$. It is expected as we used Eq. (A8) for
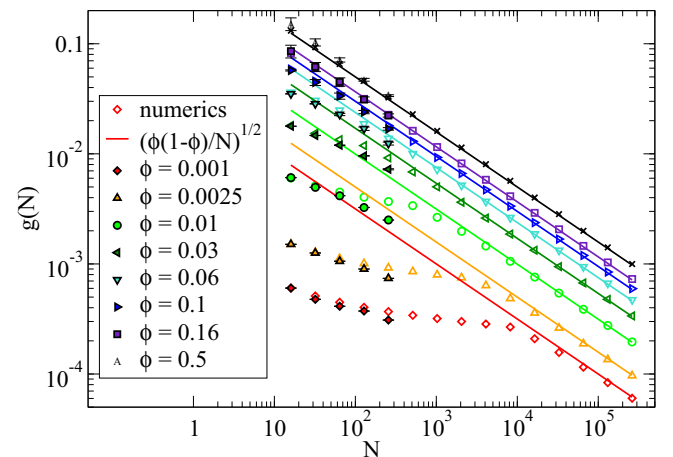

FIG. 21. Variation of the function $g(N) = (\phi - \sigma^R)/[1 + r(N)]/\sqrt{2h_N}$ with N for different values of ϕ. The solid symbols and the symbol A correspond to simulation results, with a yield stress of hard sites of $\Sigma^H = 10$. The opened symbols of the same color and same shape correspond to a numerical evaluation of $g(N)$ using 10 000 iterations of N drawings from a binomial distribution with parameters N and ϕ. The solid lines correspond to the analytical estimation given in Eq. (A19) in the limit of large N.

$O(\epsilon) = O(\epsilon/\phi) = O[\epsilon/(1 - \phi)]$. For extreme values of ϕ the analytical estimation only gives satisfactory results for very large N. The ϕ-$(1 - \phi)$ symmetry is then recovered. However, the numerical evaluation of the minimum is in very good agreement with the simulation results for all values of ϕ as is shown in Fig. 21. In this figure, the fraction f of hard sites in the weakest band is estimated from the simulation results as $\sigma^R(\phi, N) = [\Sigma^F(\phi, N) - \Sigma^A(N)]/[\Sigma^H - \Sigma^A(N)]$.

[1] S. Torquato, *Random Heterogeneous Materials. Microstructure and Macroscopic Properties* (Springer, New York, 2002).

[2] J. F. Branthaver, J. C. Pedersen, R. E. Robertson, J. J. Duvall, S. S. Kim, P. M. Harnsberger, T. Mill, E. K. Ensley, F. A. Barbour, and J. F. Schabron, Tech. Rep. SHRP-A-368. Strategic Highway Research Program (1993).

[3] D. A. Anderson, D. W. Christensen, H. U. Bahia, R. Dongre, M. G. Sharma, C. E. Antle, and J. Button, Tech. Rep. SHRP-A-369. Strategic Highway Research Program (1994).

[4] J.-S. Chen and C.-H. Peng, J. Mater. Civ. Eng. **10**, 256 (1998).

[5] T. You, R. K. Abu Al-Rub, M. K. Darabi, E. A. Masad, and D. N. Little, Constr. Build. Mater. **28**, 531 (2012).

[6] D. C. Hofmann, J.-Y. Suh, A. Wiest, G. Duan, M.-L. Lind, M. D. Demetriou, and W. L. Johnson, Nature **451**, 1085 (2008).

[7] M. Ferry, K. J. Laws, C. White, D. M. Miskovic, K. F. Shamlaye, W. Xu, and O. Biletska, MRS Commun. **3**, 1 (2013).

[8] R. Dasgupta, P. Mishra, I. Procaccia, and K. Samwer, Appl. Phys. Lett. **102**, 191904 (2013).

[9] O. Gendelman, A. Joy, P. Mishra, I. Procaccia, and K. Samwer, Acta Mater. **63**, 209 (2014).

[10] R. K. Abu Al-Rub, Int. J. Multiscale Com. **7**, 329 (2009).

[11] R. K. Abu Al-Rub, M. K. Darabi, T. You, E. A. Masad, and D. N. Little, Int. J. Roads Airports (IJRA) **1**, 68 (2011).

[12] R. K. Abu Al-Rub, T. You, E. A. Masad, and D. N. Little, Int. J. Eng. Sci. Appl. Math **3**, 14 (2011).

[13] S. Roux, D. Vandembroucq, and F. Hild, Eur. J. Mech. A **22**, 743 (2003).

[14] S. Patinet, D. Vandembroucq, and S. Roux, Phys. Rev. Lett. **110**, 165507 (2013).

[15] P. Ponte-Castaneda and G. DeBotton, Proc. R. Soc. A **438**, 419 (1992).

[16] G. DeBotton, Int. J. Solids Struct. **32**, 1743 (1995).

[17] N. A. Fleck and J. R. Willis, J. Mech. Phys. Solids **52**, 1855 (2004).

[18] S. Turgeman and B. Guessab, Mech. Res. Comm. **38**, 181 (2011).

[19] P. Suquet and N. Lahellec, Procedia IUTAM **10**, 247 (2014).

[20] V. V. Bulatov and A. S. Argon, Modell. Simul. Mater. Sci. Eng. **2**, 167 (1994).

[21] J.-C. Baret, D. Vandembroucq, and S. Roux, Phys. Rev. Lett. **89**, 195506 (2002).

[22] G. Picard, A. Ajdari, L. Bocquet, and F. Lequeux, Phys. Rev. E **66**, 051501 (2002).

[23] E. R. Homer and C. A. Schuh, Acta Mater. **57**, 2823 (2009).

[24] M. Talamali, V. Petäjä, D. Vandembroucq, and S. Roux, C.R. Mécanique **340**, 275 (2012).

[25] A. Nicolas, K. Martens, L. Bocquet, and J.-L. Barrat, Soft Matter **10**, 4648 (2014).

[26] D. Rodney, A. Tanguy, and D. Vandembroucq, Modelling Simul. Mater. Sci. Eng. **19**, 083001 (2011).

[27] A. S. Argon, Acta Metall. **27**, 47 (1979).

[28] M. L. Falk and J. S. Langer, Phys. Rev. E **57**, 7192 (1998).

[29] J. D. Eshelby, Proc. R. Soc. A **241**, 376 (1957).

[30] D. Vandembroucq and S. Roux, Phys. Rev. B **84**, 134210 (2011).

[31] E. R. Homer, Acta Mater. **63**, 44 (2014).

[32] E. R. Homer, Acta Mater. **83**, 203 (2015).

[33] M. Talamali, V. Petäjä, D. Vandembroucq, and S. Roux, Phys. Rev. E **84**, 016115 (2011).

[34] F. Spaepen, Acta Metall. **25**, 407 (1977).

[35] C. E. Maloney and A. Lemaître, Phys. Rev. Lett. **93**, 195501 (2004).

[36] A. Tanguy, F. Leonforte, and J.-L. Barrat, Eur. Phys. J. E **20**, 355 (2006).

[37] J. Ding, S. Patinet, M. L. Falk, Y. Cheng, and E. Ma, Proc. Natl. Acad. Sci. USA **111**, 14052 (2014).

[38] M. Tsamados, A. Tanguy, C. Goldenberg, and J.-L. Barrat, Phys. Rev. E **80**, 026112 (2009).

[39] Z. Budrikis and S. Zapperi, Phys. Rev. E **88**, 062403 (2013).

[40] B. Tyukodi, S. Patinet, S. Roux, and D. Vandembroucq, arXiv:1502.07694.

[41] C. E. Maloney and A. Lemaître, Phys. Rev. Lett. **93**, 016001 (2004).

[42] C. E. Maloney and A. Lemaître, Phys. Rev. E **74**, 016118 (2006).

[43] J. Lin, E. Lerner, A. Rosso, and M. Wyart, Proc. Natl. Acd. Sci. USA **111**, 14382 (2014).

[44] J. Leidner and R. T. Woodmans, J. Appl. Polym. Sci. **18**, 1639 (1974).

[45] B. Turcsányi, B. Pukánszky, and F. Tüdos, J. Mater. Sci. Lett. **7**, 160 (1988).

[46] J.-S. Chen and K.-Y. Lin, J. Mater. Sci. **40**, 87 (2005).

[47] P. Bak and K. Sneppen, Phys. Rev. Lett. **71**, 4083 (1993).

[48] J. Schmittbuhl, S. Roux, J. P. Vilotte, and K. J. Måløy, Phys. Rev. Lett. **74**, 1787 (1995).

[49] H. J. Gao and J. R. Rice, J. Appl. Mech. **56**, 828 (1989).

[50] R. Arratia and L. Gordon, Bull. Math. Biol. **51**, 125 (1989).

[51] C. Blondeau, La cryptanalyse différentielle et ses généralisations, Ph.D. thesis, Univ. Pierre et Marie Curie, Paris (2011).

[52] C. Blondeau, B. Gérard, and J.-P. Tillich, Des. Codes Crypt. **59**, 3 (2010).

[53] J. Weiss, L. Girard, F. Gimbert, D. Amitrano, and D. Vandembroucq, Proc. Natl. Acad. Sci. USA **111**, 6231 (2014).